NaaS

Chronic neurological effects and photocatalytic investigation of AZO dyes

P. Rubalajyothi [a],*, A. Rajendran [a], Lekshmi Gangadhar [b],*, V. Pandiyan [a]

[a] Department of Physics, Nehru Memorial College affiliated to Bharathidasan University, Tiruchirappalli-07, Tamilnadu, India
[b] Department of Nanotechnology, Nanodot Research Private Limited, Nagarcoil, Kanyakumari, India

ARTICLE INFO

ABSTRACT

The well-known medical participation of AZO dye industry derivatives in the use of vital brilliant red dye acts as an anticonvulsant. The AZO dyes permeability through the blood–brain barrier was found to be a factor in the development of a vast variety of chronic neurological diseases. Because of the potential influence on the environment and human health, the presence of AZO dyes in textile effluents is a major concern. Under visible light, we analyze the photocatalytic degradation of AZO dyes, which are widely utilized in the textile sector. In the present analysis, the properties of combustion-formed mixed sulfide solids were investigated in solutions which are supersaturated simultaneously with dysprosium and erbium. The $Sr_{1-x}Cu_xSO_4$ nanoparticles arrangement acts as a step for dysprosium and erbium co-doping based on the interactions between thiourea. The phase structure and sample states obtained of the stimulant components be analyzed by Field emission scanning electron microscopy (FESEM), High-resolution transmission electron microscopy (HR-TEM) and photosynthetic studies with X-ray powder diffraction (XRD) and Fourier-transform infrared spectroscopy (FTIR). Additional data analysis by Rietveld refinement allowed the exposure of a smaller lattice parameter and volume increase related to the absorption of stimulant components. Integrated $Sr_{1-x}Cu_xSO_4$ co-doped Dy^{3+}, Er^{4+} showed effective photosynthetic presentation at some stage in decomposition of organic dyes (Acid Black 1, direct blue 15), and hydrogen production from water under ultraviolet light. In addition, Dy, Er co-doped was also deposited and their photosynthetic activities were examined. The consequences and impact on neurology are also examined in this article.

1. Introduction

The use of fundamental technologies focused on photosynthetic processes is one of the most exciting ways of solving the extensive problems of renewable energy and the climate. Due to its optical properties, chemical stability, non-toxicity and high photosynthesis, Catalyzed TiO_2 has attracted significant interest. Consequently, this type of material is widely used for the decomposition and combination of many organic compounds [1,2]. Recent technologies have released many heavy metals into the environment and they cause serious problems [3]. Water pollution can lead to changes in physical, chemical and biological standards [4]. The presence of copper, zinc, lead, iron, nickel and other metals can cause harm to human physiology and other biological systems when the tolerance level is exceeded [5]. Concentrations of heavy metals less these limits have the potential for long-term pollution because heavy metals accumulate within biological systems [6]. Many industrial and metallurgical processes, such as plating, photography, aviation, nuclear and petrochemical facilities, have emitted heavy metals into the environment and polluted water resources [7–11]. Heavy metals such as lead and cadmium create a serious threat to living organisms, and concentrations are very low due to mutation carcinogens and accumulating properties [12–18].

CuO is a P-type semiconductor with a band gap of 1.21–1.51 eV and a monoclinic structure [19–21]. It is an interesting multifunctional material due to its photosynthetic and photochemical properties in gas sensors [22,23], magnetic storage media [24], lithium ion batteries [25] and solar cells [26]. Cu-core / $CuSO_4$-shell nanoparticles exhibited higher photosynthetic efficiency versus Cu nanoparticles, and these findings showed that the degradation of Methylene blue was significantly affected by the $CuSO_4$-
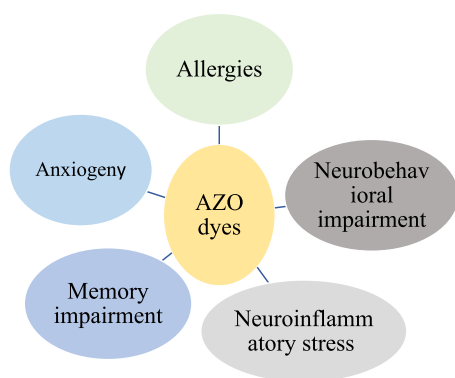
Fig. 1. Side effects of AZO dyes.

shell [27]. Numerous environmental pollutants and carcinogenic dyes are emitted by the textile and paper industries [28]. These dye contaminants are chemically stable, so technologies related to direct ultraviolet photosynthesis and hydrogen peroxide oxidation are not effective in removing color dyes. Ingestion of colorful sweets containing AZO dyes causes recurrent reactions accompanied by urticaria, angioedema, headaches, dyspnea, loss of consciousness, and abdominal pain that were not eradicated, but were instead exacerbated, by various treatments with antihistamines and intravenous corticosteroids [56–60]. Side effects of AZO dyes are shown in Fig. 1. Currently, the photosynthetic system is attracting considerable attention due to its effective colonization of dyes [29].

The Perovskite-type phase material is highly capable of many energy transfer processes due to its versatile structure and diverse properties. $SrTiO_3$ is a popular multi-metal oxide (perovskite-type) and, due to its unique chemical properties and physical properties, has attracted a lot of attention from researchers today [30–36]. $SrTiO_3$ has benefited from the durability, high chemistry and thermal stability and good catalytic activity of electron-hole pairs. In the field of research on legends and applications, $SrTiO_3$ nanostructures are therefore very important. In recent literature, several research papers on semiconductor water separation can be found [37–39]. Since CB's band border is more than 200 MeV negative compared to TiO_2, $SrTiO_3$ provides positive water separation energy. However, data on the photosynthesis pathway of $SrTiO_3$ and recent achievements and improvements in the separation of water are not yet available. In several techniques, such as hydrothermal, sol-gel and solid-state reaction (SSR), $SrTiO_3$ can be prepared, but various synthesis pathways lead to different morphology, crystallinity, uniformity, size and shape of $SrTiO_3$ nanoparticles [40,41]. The problem with the $SrTiO_3$ photo synthesizer, however, is still the wide band gap energy, which is noticeable and cannot meet the sunlight applications requirements. As a consequence, $SrTiO_3$ structural modification has been widely used to boost water separation efficiency, such as bonding with nanostructures, ion stimulants and other semiconductors. Nanomaterials have another significant application in the regulation of human pathogenic bacteria, in addition to nano-mediated photosynthetic action. In addition, for drug design and its target distribution in the affected physiological system, applications for nanomaterials can be effectively explored.

In the present analysis, the properties of combustion-formed mixed sulfide solids were investigated in solutions supersaturated simultaneously with dysprosium and erbium. The reason for this investigation was the preparation of co-doping strontium copper sulfate for dysprosium and erbium polycrystalline powders with improved stability and photocatalytic properties characteristics, using a simple technique in which the specifications of preparation were used. Improving the catalytic activities of ma-

terial properties also expected to widen their range of applications. Present study highlights the application module undermined, and encompasses assessment of photocatalytic efficiency (using UV-visible near infra-red spectroscope) of the synthesized and opto-physically characterized $Sr_{1-x}Cu_xSO_4$ co-doped Dy^{3+}, Er^{4+} nanoparticles (NPs) to using the acid black and direct blue dyes. As a model organic pollutant, was investigated in presence of visible light considering effective parameters.

2. Materials and methods

All the chemicals were obtained from Merck (99%) etc., and used without any further purification. Distilled water was used thought out the experiment. In order to prepare the following composition: $Sr_{1-x}Cu_xSO_4$:Dy^{3+}, Er^{4+} with the mol% of (x = 0.03, 0.05, 0.07, 0.09) which means Strontium nitrate and Copper sulphate dehydrate with stoichiometric (1:1ratio) and Co-doping for Dysprosium and Erbium concentrations are increased up to (0.5, 1, 1.5, 2.0). The powders were prepared by using the raw materials and added the fuel materials (urea) were successfully prepared by combustion method. Stoichiometric concentrations of barium nitrate ($Sr(NO_3)_2$) and calcium nitrate ($CuSO_4.4H_2O$) were dissolved at room temperature in an aqueous urea solution with regular stirring. Using the 80^oC magnetic stirrer, the paste level was sub-maintained to move the dried quartz crucible for 30 minutes at 500^oC. Collect the powder using the agate and grain with a fine powder. The integrated $Dy^{3+}Er^{4+}$ co-doped $Sr_{1-x}Cu_xSO_4$ powders recognized the stage arrangement by powder x-beam diffraction strategy utilizing an 'X' Perky Expert PAN analytical diffractometer utilizing Cu-Kα worked at 40 kV and 30 MA. The example was examined in the 2θ extending from 10 to 80° for 2s in the progression check mode.

For assurance of precious crystal structure, a test was examined by X-beam diffraction. The surrounding temperature photoluminescence spectra were gotten by Hitachi f-4500 fluorescence spectrophotometer furnished with xenon light. Optical ingestion spectra were estimated at room temperature utilizing Hitachi U-3010-DRS spectrophotometer. The surface morphology was analyzed by checking the electron magnifying instrument. SEM micrographs and arrangement examination of tests were gotten on a Hitachi S4800 checking electron magnifying instrument prepared. SEM estimations were mounted on aluminum reflects about utilizing glue graphite tape and sputter covered with gold before investigation. The photoluminescence outflow spectra of the examples were recorded utilizing a fluorescence spectrometer (Hitachi f-4500). A similar measure of the test was utilized for each situation. Emanation and excitation spectra were recorded utilizing a ghastly opening width of 1.5 nm.

3. Results and discussion

3.1. X-ray photoelectron spectroscopy (XPS)

The photoelectron spectra are obtained with the source gun A = X-ray 014 400um - FG ON (400 m). These are created from a mono chromatic X laser using radiation. Check the spectrum of the powders under investigation. In high impact mode, running such a spectrum allows the primary lines of all the components shown on the surface layer of the object to be considered. All the peaks are described by the electronic dimensions of dysprosium, barium, calcium, sulfur and oxygen in the arrangement of exceptional earth-soluble substances under analysis.

$Sr_{1-x}Cu_xSO_4$: Dy^{3+}, Er^{4+} in order to gain insight into the chemical environment of lanthanide an element, a study was carried out of appearance powders through X-ray photoelectron spectroscopy (XPS). The scoping review in Fig. 2 showed the peaks correlated
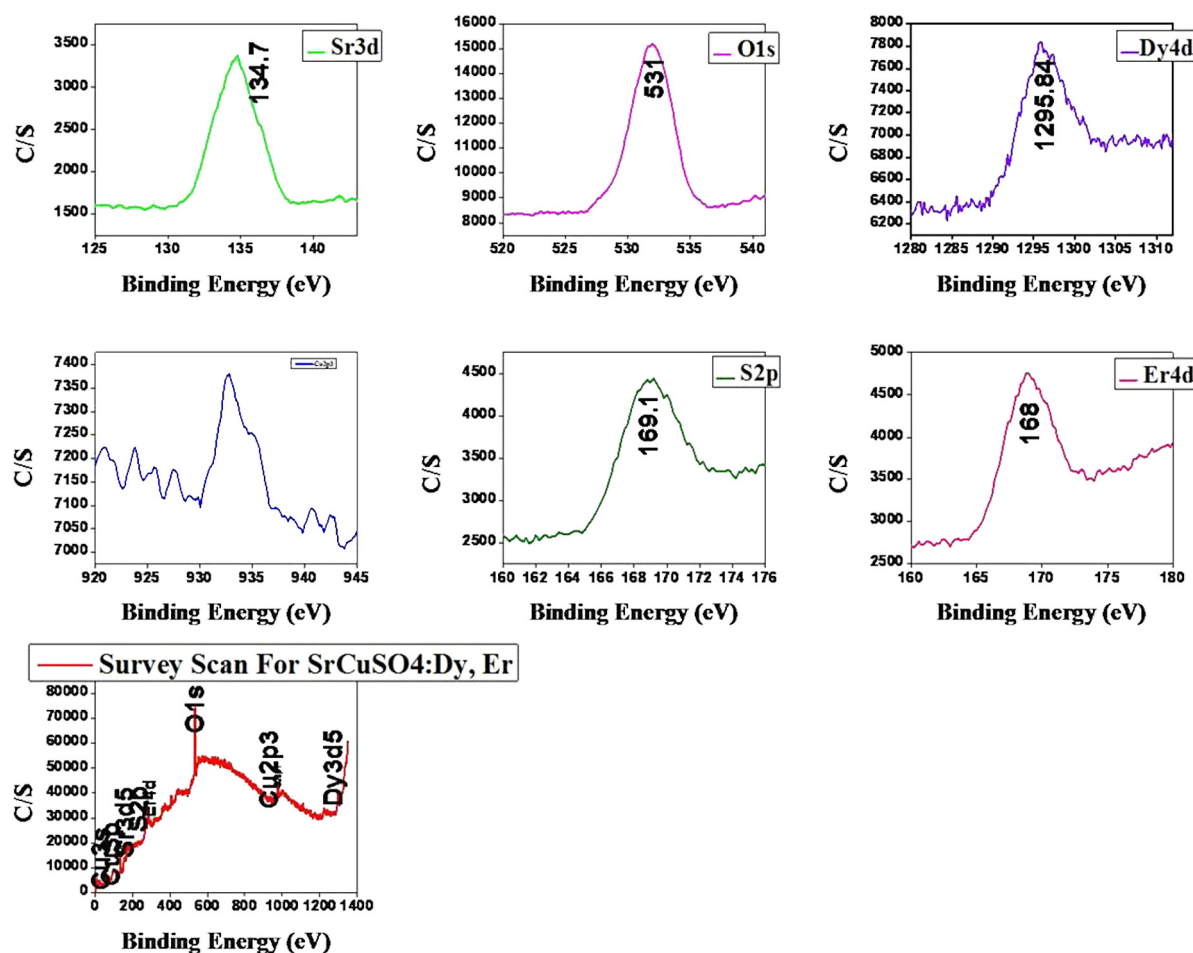
Fig. 2. XPS studies for strontium copper sulphate co-doping for lanthanide elements.

with the Sr, S, O, Dy, Er and Cu XPS range. The XPS spectrum of high resolution correlated with Sr binding energies is shown in Fig. 2. The peak study of Sr3d signals with mixed Gaussian-Lorentzian profiles shows that the fundamental components of the bonding energies are exposed at 134.7 eV [42,43]. In order to investigate Cu surface oxidation, the Cu $2p_{3/2}$ fundamental level was used. The principal satellite peaks of the Cu $2p_{3/2}$ and Cu $2p_{1/2}$ models are found. Based on the amplitude of the Cu $2p_{3/2}$ main peak, this range is normalized. Two semiconductor phases, namely cupric oxide (CuO) and cupric oxide (Cu_2O) [44], may be present in copper oxide.

In addition, the Sulfur 2p standard adopts a similar integrated Gaussian line format to the 2.79 EV FWHM. Sulfur 2p, which controls the availability of life, provides dynamically oxidized natural sulfur through material characteristics and corrects its forms, e.g. sulfoxides - (166 eV), sulfones - (168 eV) and sulfonic corrosive / sulfate - (169 eV) in S2p obverse, oxidized to S2p resolution and currently regulates 170 eV strength. O1s peaks such as 533.1 eV are assigned to the oxide from the denoising observations in the O1s XPS spectrum. 1296.4 eV is correlated with a lower energy peak at 1294.5 eV, close to the baseline stage, and Dy_2O_3 [45]. The Er4d spectrum is an erbium metal which is relatively oxygen-free. The maximum elevation ratio of Erbium (168 eV) is found under this condition. At 167.4 eV binding energy, the peak of $4d_{5/2}$ occurs, while at 175.0 eV the peak of $4d_{3/2}$ takes place. In the manual, the strength of the $4d_{5/2}$ peak is less than and remains unsolved. The energy separation of 7.6 eV between $4d_{5/2}$ and $4d_{3/2}$
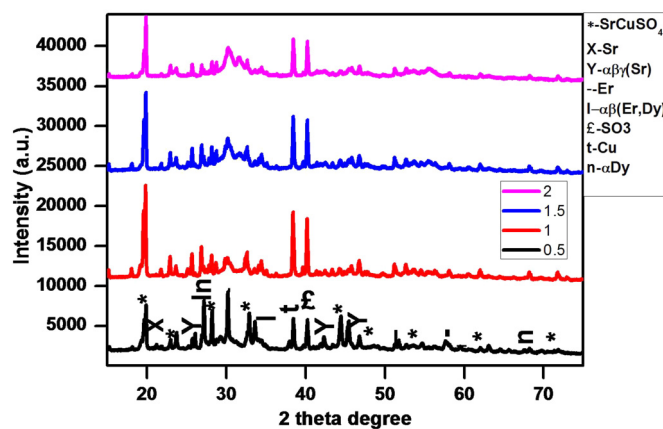

Fig. 3. X-ray diffraction studies for to find the crystal structure and crystal size.

peaks is [46], in good agreement with the theoretical value mentioned in the literature.

3.2. XRD

The nanocrystalline $Sr_{1-x}Cu_xSO_4$ doped Dy^{3+}, Er^{4+} in X-ray diffraction experiments. All XRD peaks reflect the orthorhombic system's single phase structure. Following the Scherer formula, crystal sizes are determined, and the crystal size is 25 to 35 nm. This orthorhombic form of the doped Dy^{3+}, Er^{4+} type structure of
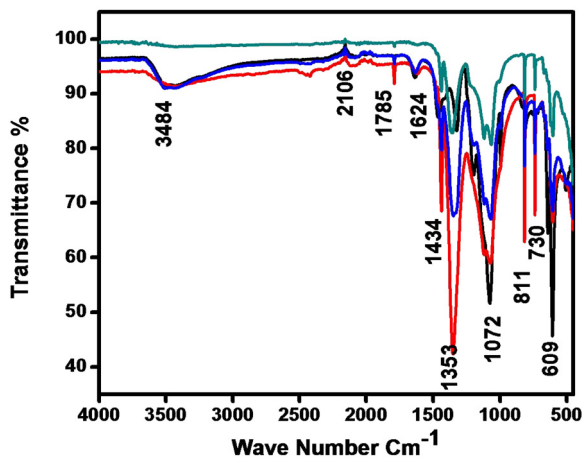
Fig. 4. Functional analysis for FTIR Spectroscopy.

$Sr_{1-x}Cu_xSO_4$ is heated at 500^oC. XRD data of $Sr_{1-x}Cu_xSO_4$ doped Dy^{3+}, Er^{4+} powders with varying quantities of rare-earth ions indicate structures without any contamination, with all orthorhombic peaks found with the Pmmm space group shown in Fig. 3.

3.3. FTIR

The peak at 3484 cm^{-1} is attributed to the presence of alcohols, phenols with O-H symmetric stretching; the peak at 2106 cm^{-1} is present in the form of alkenes with -C (triple bond) C- stretching vibration; and the peaks at 1785 cm^{-1} C=O stretching respectively of carbonyl, carboxyl and acetyl groups and ofxylans. In Fig. 4, combination signals of 1624 and 1434 cm^{-1} were observed suggesting the interaction of alkenes' -C=C- stretching vibration presence, C-H bends stretching alkenes' vibration presence in the composite. Due to the N-O stretching vibration presence of nitro compounds, the peak at 1353 cm^{-1}, the signal at 1072 cm^{-1} is related to the aliphatic amine phase C-N stretching vibration presence. N-H wags stretching vibration presence of major, secondary amine products are generally observed at the peak at 811 cm^{-1}; 730 and 609 cm^{-1} this signal may be attributed to the presence of C-H rocking of >CH$_2$ in alkyl halides fatty acids, proteins, C-Br stretching mode presence.

3.4. Photoluminescence

In Fig. 5, all work changes related to excitation and emission spectrum are present in the photovoltaic excitation and emission spectrum associated with Dy^{3+}, Er^{4+} particles measured in $Sr_{1-x}Cu_xSO_4$. Nature is sensitive and very rare, after all. This proves that development can easily be influenced by such a move. The structural data of the substitute character obtained by the highlight X-beam differential can be given by this strength. Somewhere in the 450 and 650 nm range, there are split ends that are comparable to the Intra-4F-shell, which differs from the $^5D_0$ energy stage. The $^5D_0$-$^7F_2$ power shift with DJ = 2 is easily affected by power level demands and continues in the neighboring environment [47]. In the photovoltaic excitation range, the range of excitation due to radiation enhancement can be calculated. No significant matching exchange between the subject and the host has been reported to exist [48,49]. One of the attractive results of this work is that modified UV activation in phosphorus will definitely stimulate the excitation limit of Dy^{3+}, Er^{4+} doped $Sr_{1-x}Cu_xSO_4$ phosphor. Higher peaks are associated with an increase in Dy^{3+}, Er^{4+} levels by shifting the levels of excitement to broader groups. Areas of relative care and related forces correspond to the excitation range. Similarly, the host or Dy^{3+}, Er^{4+} -O2 - charge-transfer are found in

sharp iridescence and small wavelength extension. In addition, this miracle ensures that Dy^{3+}, Er^{4+} connections with the host phase are powerless and that no power transfer occurs between Dy^{3+}, Er^{4+} and the host [50].

Fig. 5 display the photovoltaic excitation and emission spectrum of $Sr_{1-x}Cu_xSO_4$ (X = 0.03, 0.05, 0.07, 0.09). At emission wavelengths of 594, 688 and 729 nm, the insurgent spectrum based at 392 nm is observed. For $Sr_{1-x}Cu_xSO_4$ at 392 nm, Fig. 5 shows a solid, asymmetrical, and broad emission band at 594 nm. A change in the 4f - 4f state is correlated with this Dy^{3+}, Er^{4+} emission. There are two Gaussian components of the asymmetric emission band, 688, 729 nm (red, SrO_{10}) and 594 nm (yellow, SrO_9), reflecting the two emission centers in the S2S lattice. In contrast, for x= 1.5 mol %, the emission band at 594 nm is very high. If the amount is increased to X = 0.5, 1, 1.5, 2 mol %. With a speed of 570 nm, the peak subsided and dominated. This clearly shows the change from the SrO_{10} to SrO_9 base of the emitter core when transforming massive Er^{3+}, Sr^{2+}. SrO_{10}'s average Sr-O bond length (2.86) is greater than that of the SrO_9 (2.17 Å) base, which, when stimulated at the latter site, induces a relatively large shift. A broader emission, but not the edge range, is shown by the entire PL absorption spectra (250-500 nm), suggesting no change in the oxidation state of the Dy^{3+} and Er^{4+} ions. The emission moisture seen when the X value is increased may be due to differences in the ion radius and electro negativity of Dy^{3+} and Er^{3+} compared to Sr^{2+} ions [51]. Converting small amounts of Dy^{3+}, Er^{4+} into host lattice collection leads to decomposition into crystal lattice [52] The oxidation state remains the same. Furthermore, Dy^{3+}, Er^{4+} dominate the constituting constant control factor over S2S, while S2S has Dy^{3+} and Er^{4+} generating components. Although the increasing dopant level of Dy^{3+} controls the emission of luminescent from yellow to red, the change in element transition is not always optimal for enhanced luminous intensity, especially in our case. This will be the key limitation and sensitivity solution for improving emissions when adjusting luminous emission via the crystal site engineering approach.

For $Sr_{1-x}Cu_xSO_4$, 0.5, 1, 1.5, 2% for Dy^{3+}, Er^{4+}, the excitation is found at a maximum of 392 nm while at an emission wavelength of 594 nm. Compared with Dy^{3+} (Ex = 392 nm), the excitation wavelength is significantly red shift. This change may be due to a change in the observation emission wavelength from 594 to 729 nm. In addition, Er^{4+} naturally absorbs low-energy photons and emits a broad elastic spectrum on the high-wavelength side. At X (Dy^{3+}, Er^{4+}) = 0.5, 1, 1.5, and 2%, the radical group also turned red at 429 nm and exhibited a much wider and shoulder peak around 392 nm. R_C is the inherent neutrality between the donor and the acceptor, with an internal orbital radius for which there are non-radioactive exchange rates. Blasse agreed that the usual compression closest to the fundamental focus between the activator particles is identical to the fundamental separation. In many minerals, according to Dexter's hypothesis, focusing sometimes does not occur due to electrical / attractive multi-polar cohesion between activator particles comparable to those in the host. From these conditions, the basic separation from the fixation extinguishing information utilizes the accompanying condition:

$$R = (3V/4\pi X_C N)^{1/3} \qquad (1)$$

Where X_C is the critical concentration, N is the number of Dy^{3+} ions in the $Sr_{1-x}Cu_xSO_4$ in that unit cell; V is the volume of the unit cell. The critical concentration is also estimated.

3.5. FESEM with mapping

The best analytical tools for structural and morphological characteristics are SEM. Fig. 6 shows that the formation of Nanopar-
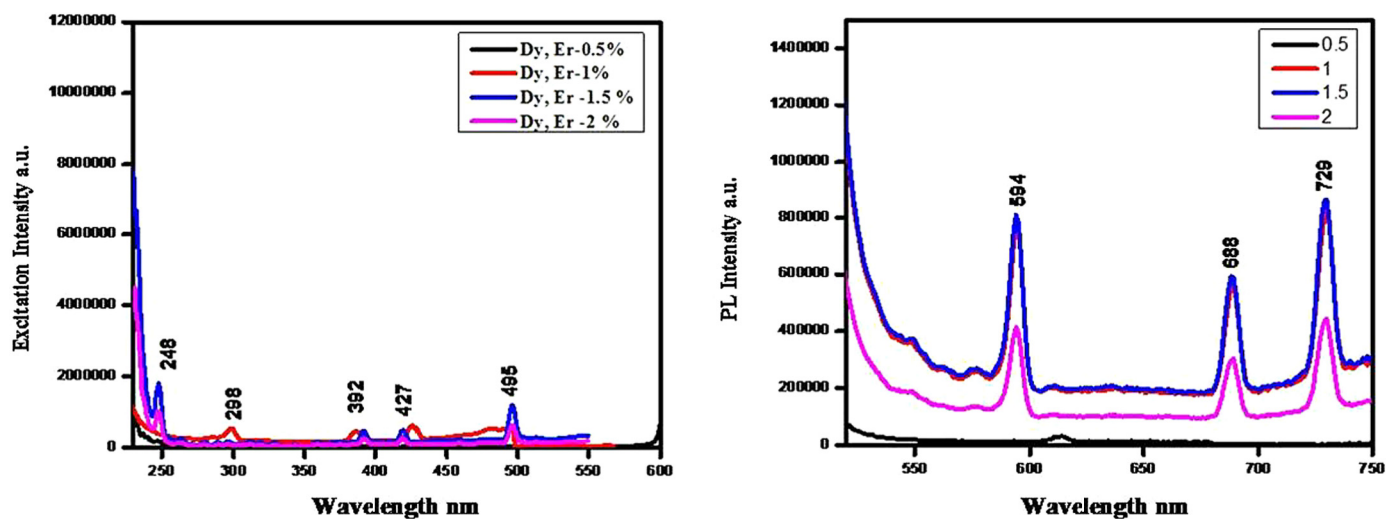
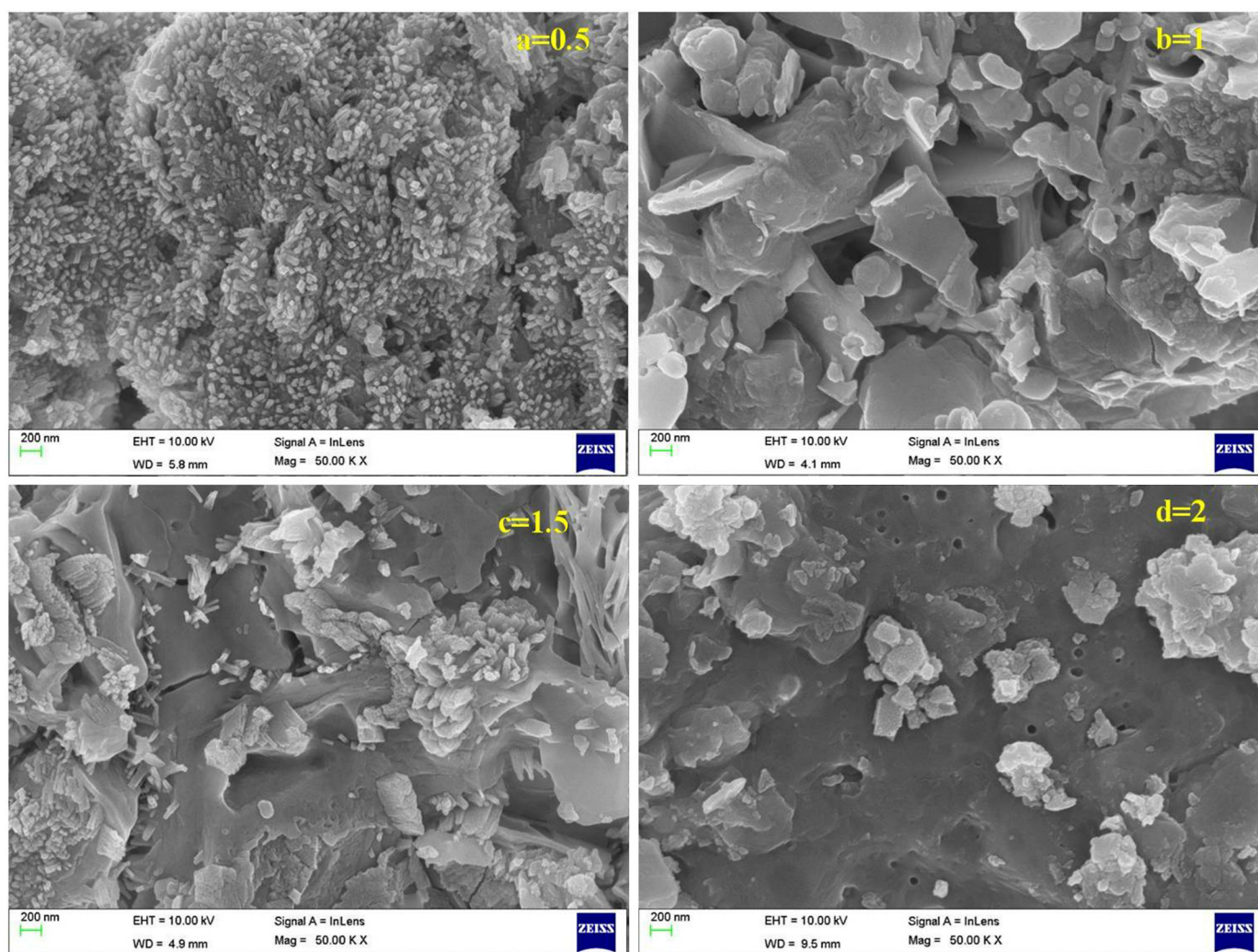**Fig. 5.** Photoluminescence studies.

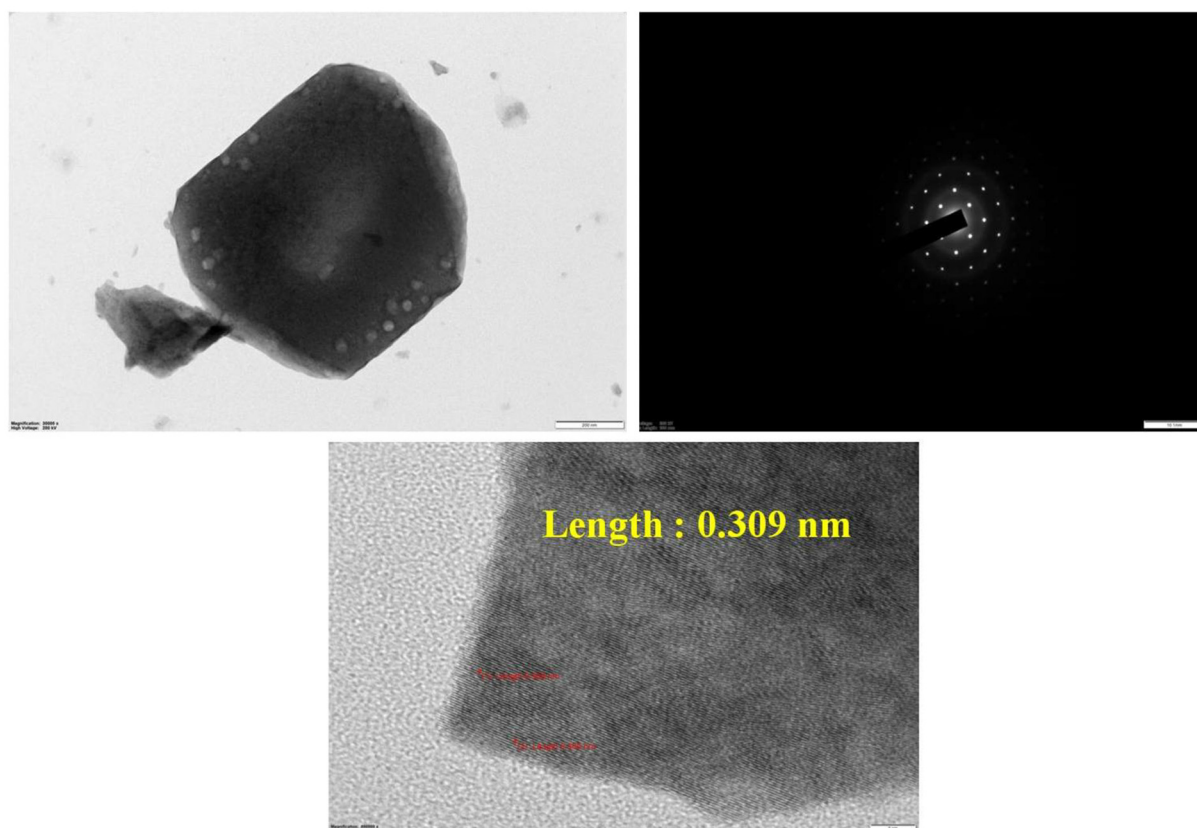**Fig. 6.** FE-SEM analysis to find the morphological studies for nanomaterials.

Fig. 7. HR-TEM of $Sr_{1-x}Cu_xSO_4$ particles.

ticles prompted dysprosium, erbium to analyze $Sr_{1-x}Cu_xSO_4$. Most particles have a rod shape. And the same kinds of granules are also found. As illustrated in the material fragment of the material is further shown by their nuclear affinity and character. It then scans for particle analysis to detect shape and size, presenting an important natural presence to derive from diffraction spectroscopy information. The collective structure of each component is highly integrated. The new interesting results of rod shape created in dysprosium and erbium doping for 0.5 mol%. The doping materials are increased the SEM image is clearly in bore shape is created.

3.6. HR-TEM with SAED pattern

HRTEM images Fig. 7 show that the sample was composed of both isolated and aggregated particles. The morphology of $Sr_{1-x}Cu_xSO_4$ particles is nearly close to two types of structure to compare the XRD studies like the spherical and orthorhombic irregular in shape with moderate variation in size figure. The size determined diameter between 275-371 nm with an average diameter size of 326 nm.

In Fig. 7 HRTEM analysis shows that lattice fringes with an in interplayed distance of 0.309 nm is close to the 0.3531 nm lattice spacing of the 002 crystal planes of barite phase. This was confirmed by Fast Fourier Transformation (FFT) patterns, which is also in accordance with XRD results. For this study, noise reduction was performed on the square labeled area. The high dispensability of the powder in water might be related to the particles. In order to verify the crystalline nature of the nanoparticles the selected area electron diffraction (SAED) patterns were obtained for the sample containing dysprosium doped barium calcium sulphate for different regions and particles. The results of SAED pattern are also analyzed.

3.7. Photocatalytic

3.7.1. Acid black 1(AB1)

To research the photocatalytic properties of synthesized nanoparticles in the degradation of organic materials, Acid Black 1 was used. Towards this end, the samples were prepared at a concentration of 20 mg/l and exposed to UV light with a light intensity of 30 mins of initial concentration, natural pH and nanomaterials within defined conditions. The samples were held in darkness for 30 mins and afterwards exposed to light in order to identify the absorption and consequence of light on the dye decomposition processes. After exposure to darkness and light, the absorption samples were measured at a wavelength of 613-616 nm, in Fig. 8.

Both catalysts were also found to have greater efficiency and darkness in the presence of light. Opposing to the standards of doped Dy^{3+}, however, Er exhibits a strong affinity for AB1 oxidation. Since in acidic condition, doped Dy^{3+}, Er^{4+} NPs are positively charged by electrostatic interaction adsorbing AB1 molecules, whereas in alkaline condition they are negatively charged and due to repulsive forces the adsorption of AB1 molecules is poor. This behavior of adsorption and activity can be based on many variables, and indicates that there are also other interactions between AB1 and the doped Dy^{3+}, Er^{4+}, regardless of the charge distributions. The possible mechanisms for adsorption of AB1 on doped Dy^{3+}, Er^{4+} (lanthanide elements) NPs can therefore be connected to the presence in the structure of AB1 of several functional groups. Such groups may be charged and the degree of electrostatic interactions may increase [53]. On the other hand, the presence of donors and acceptors of hydrogen bonds in AB1 shows the levels of interaction with hydrogen between AB1 and doped lanthanide NPs. In addition, the interaction of vander Waal's and hydrophobic interactions among AB1 and doped Dy^{3+}, Er^{4+} NPs
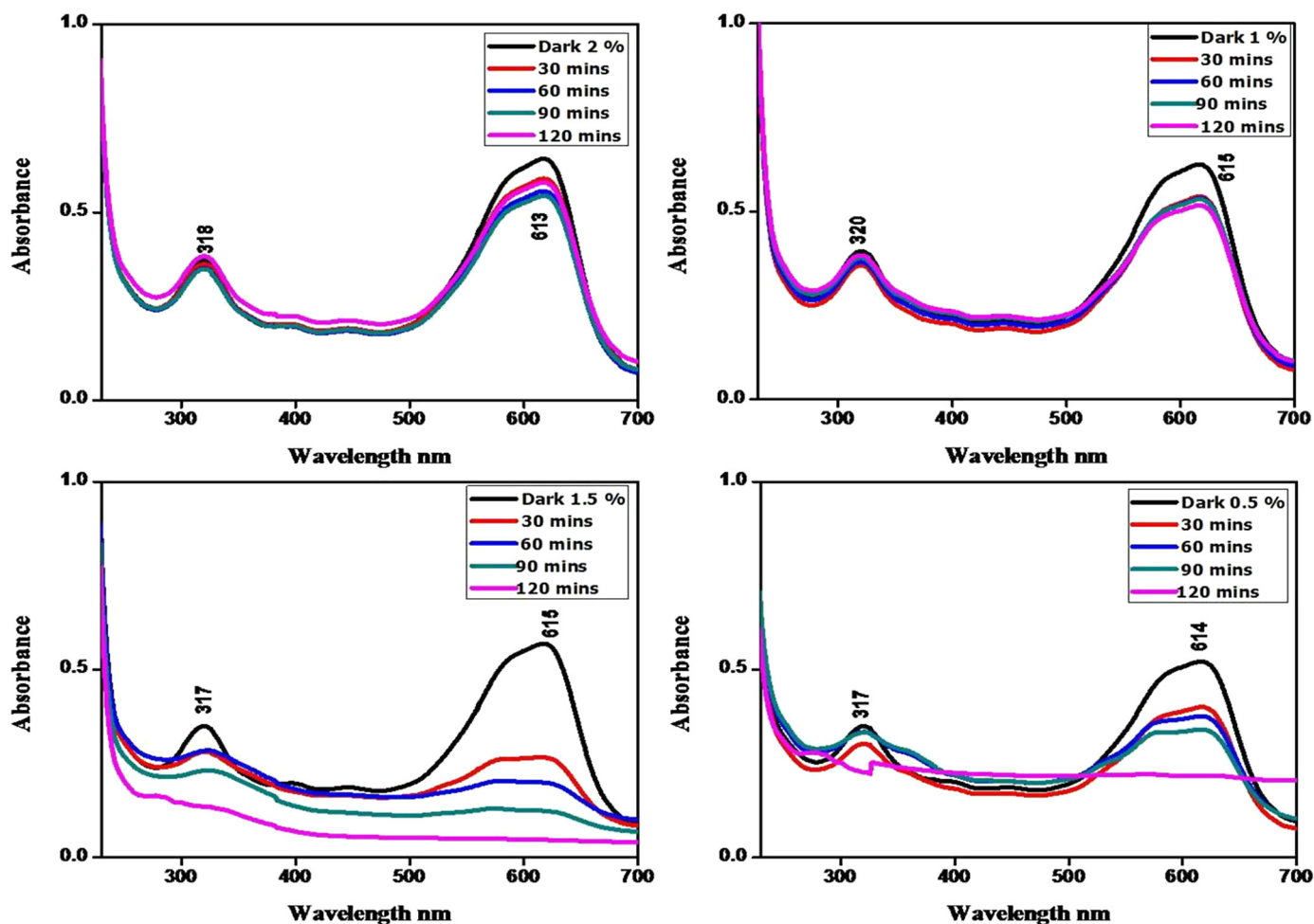
Fig. 8. Acid black 1 to using the studies for $sr_{1-x}Cu_xSO_4$ co-doping for photocatalytic activities.

are another factor that may be involved in the process of adsorption. Similar findings have been reported during the photocatalytic degradation process for dye adsorption [54,55].

The maximum dye removal efficiency in the presence of UV light was presented by $Sr_{1-x}Cu_xSO_4$ doping Dy^{3+}, Er^{4+} nanoparticles. The explanation for this is due to the generation in the presence of both light and catalyst of reactive species. In addition, the $Sr_{1-x}Cu_xSO_4$ band gap energy can be decreased by doping nanoparticles, and catalytic performance can be increased and activated in visible light. The removal efficiency of the acid black 1 dye was very low and about 0.21-0.04% in the study of the use of Ultraviolet rays alone. This suggests that the manufacture of hydroxyl radicals plays a major role in the onset of dye decomposition, which involves catalysts to absorb them. This also indicates that the presence of both the catalyst and UV emission has been the most significant factor in activating and accelerating the photocatalytic reaction.

3.7.2. Effect of nanoparticles amount on photocatalytic degradation of dye

Due to economic costs, the amount of nanoparticles used in the process is one of the most important elements in photocatalytic technology. In the analysis of the effect of $Sr_{1-x}Cu_xSO_4$: Dy^{3+} on the mechanism of photocatalytic degradation of dye, dosage of Er^{4+} nanoparticles, samples with a dye concentration of at natural pH and nanoparticles, 20 mg/L were exposed to UV lamps at different ratios of 0.5,1,1.5 and 2 mol%. The samples were tested at 613-616 nm after 30 minutes in terms of absorbance and efficiency of removal. The findings are presented in Fig. 9. It demonstrates

that increasing the dosage of nanoparticles improves the efficiency of dye removal, so that 0.21-0.04% absorbance was the percentage of removal for the nanoparticles dosage of 0.5, 1,1.5 and 2 mol%. Increasing the amount of catalyst increases the active surfaces of the catalyst, thereby increasing the development of hydroxyl radicals and other oxidation reaction radicals in this process.

Previous studies have also shown that the increase in the quantity of nanoparticles to a certain degree directly affects the efficiency of removal and, higher than a certain value, may not have a positive impact on the efficiency of removal, but may decrease the efficiency as a consequence of the disruption of the suspended particulate light pathway. As the catalyst content increases, the amount of photocatalytic degradation increases, resulting in an increase in active catalyst surfaces and, subsequently, an increase in the development of hydroxyl and superoxide radicals.

3.7.3. Effect of initial concentration of dye on photocatalytic degradation of dye

Specimens of different concentrations were prepared and exposed to UV light for 30 minutes in order to determine the effect of the initial dye concentration on the photocatalytic removal process. The samples were then centrifuged and the absorbance at 613-616 nm was measured and the efficiency of removal was determined. The explanation for this may be that more active catalyst surface sites are protected by an increase in the initial concentration of the pollutant, which decreases the production of oxidizing radicals and eventually contributes to low decomposition. Increased concentration of pigment induces decreased light penetration, increased adsorption of dye on the catalyst surface, and
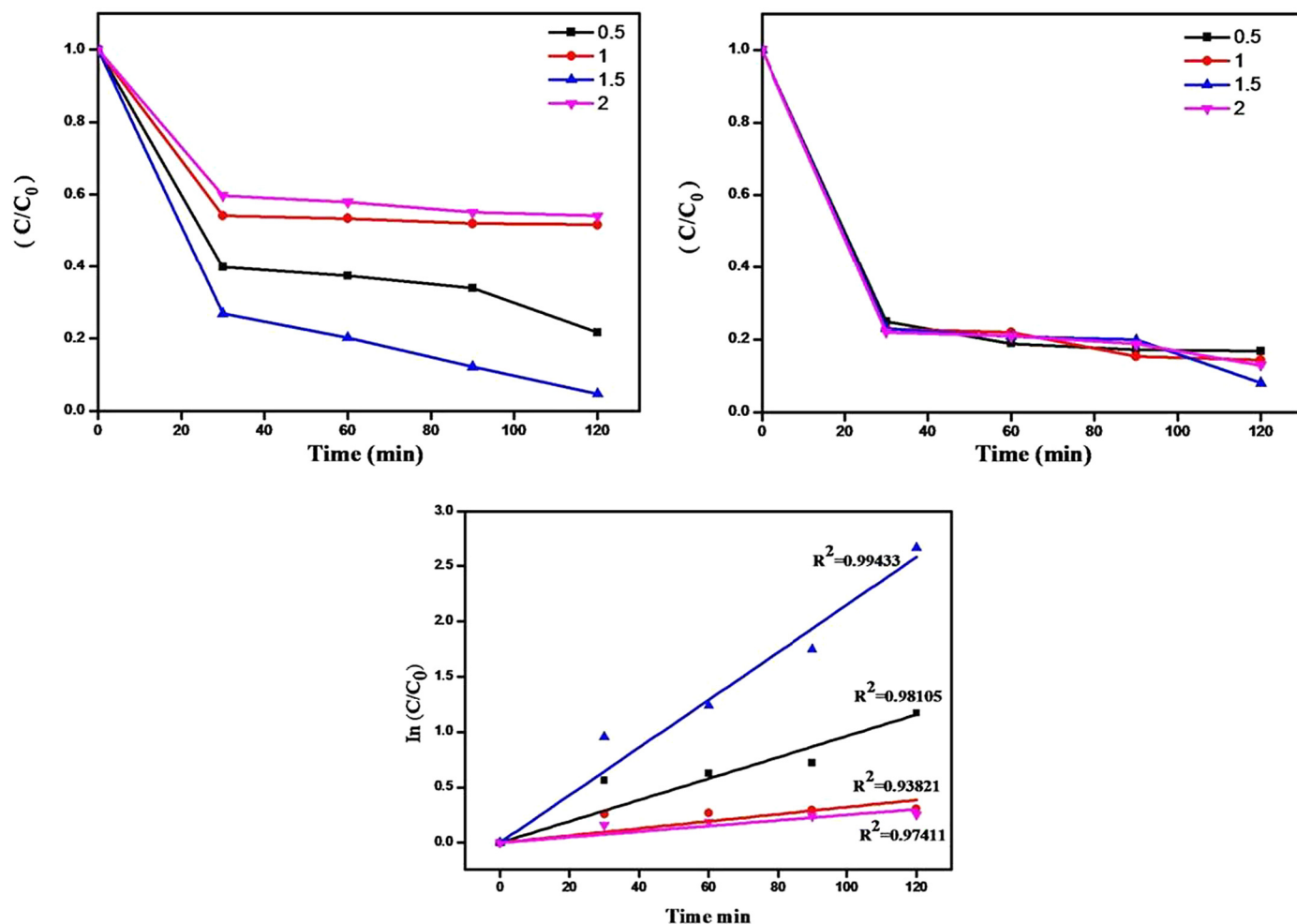
Fig. 9. Photocatalytic studies for acid black 1(AB1) c/c0 dye degradation.

occupation of the surface sites of nanomaterials by dye molecules. In our case, the doping quantity of dysprosium and erbium with a 0.5 and 1.5 percent mol quantity was very efficient compared to 1 and 2 mol% removal efficiency. In this, one of the successful degradation of removal dye in AB1 was concluded.

4. Conclusion

The efficient synthesis of $Sr_{1-x}Cu_xSO_4$ Doping Dy^{3+}, Er^{4+} nanocomposites was obtained using the combustion method on the basis of XRD, FTIR spectroscopy, XPS, photoluminescence, photocatalytic activities and TEM results. The measurements show that the material acquired corresponds to Dy^{3+}, Er^{4+} doping $Sr_{1-x}Cu_xSO_4$ nanocomposites with particle size below 35 to 45 nm. After 30 min of UV irradiation using acid black 1 initial concentration of 100 mg/L and a catalyst load of dye initial concentration, $Sr_{1-x}Cu_xSO_4$ doping Dy^{3+}, Er^{4+} particles revealed only 0.21-0.04 percent of acid black 1 dye photodegradation, the efficiency was 0.21-0.04 percent and also the same method for using the Direct blue 15. In summary, the results of the present study show that $Sr_{1-x}Cu_xSO_4$ doping with dysprosium and erbium nanocomposites decreases the elimination of catalytic efficiency by promising effective Photocatalysis for the degradation of organic pollutants such as black acid 1 and direct blue acid. It is easier to compare the two forms of black dye acid 1 than direct blue 15. One of the most common routes for dye absorption into humans is through the usage of AZO dyes in the textile industry. Irrigation may have deposited the AZO chemicals in the agricul-

tural land. However, AZO dyes significantly provoke the release of oxido-nitrergic and neuroinflammatory stress markers and also may incite acetyl-cholinesterase activities in different brain regions leading to memory and neurobehavioral impairment. Convulsions are rare when a small amount of dye is absorbed in the intact brain. A shift in the pressure connections between the blood in the brain veins and the tissue-fluid in the surrounding nerve material could explain the enhanced dye absorption. In future, total removal of dyes from food cycle is to be designed.

Declaration of competing interest

The authors declare no conflict of interest.

Acknowledgement

References

[1] S. Ivanov, A. Barylyak, K. Besaha, A. Bund, Y. Bobitski, R. Wojnarowska-Nowak, et al., Nanoscale Res. Lett. 11 (2016) 1.
[2] G. Tian, H. Fu, L. Jing, C. Tian, J. Hazard. Mater. 161 (2009) 1122.
[3] J. Tomko, M. Backor, M. Stofko, Acta Metall. Slovaca 12 (2006) 447.

[4] A.J.M. Barros, S. Prasad, V.D. Leite, A.G. Souza, Bioresour. Technol. 98 (2007) 1418.
[5] Z.R. Holan, B. Volesky, Bioresour. Technol. 43 (1994) 1001.
[6] S.Y. Quek, D.A.J. Wase, C.F. Forster, Water SA 24 (1998) 251.
[7] Z. Al-Qodah, Desalination 196 (2006) 164.
[8] S. Congeevaram, S. Dhanarani, J. Park, M. Dexilin, K. Thamaraiselvi, J. Hazard. Mater. 146 (2007) 270.
[9] N. Das, R. Vimala, P. Karthika, NIScPR Online Period. Repos. 07 (2008) 159.
[10] M. Kobya, E. Demirbas, E. Senturk, M. Ince, Bioresour. Technol. 96 (2005) 1518.
[11] F.J. Alguacil, A. Cobo, M. Alonso, Chem. Eng. J. 85 (2002) 259.
[12] M. Sadrzadeh, T. Mohammadi, J. Ivakpour, N. Kasiri, Chem. Eng. Technol. 144 (2008) 431.
[13] P. Canizares, A. Perez, R. Camarillo, Desalination 144 (2002) 279.
[14] X.J. Yang, A.G. Fane, C. Pin, Chem. Eng. J. 88 (2002) 37.
[15] D. Pathania, G. Sharma, R. Thakur, Chem. Eng. J. 267 (2015) 235.
[16] R. Kumar, M. Kumar, R. Ahmad, M.A. Barakat, Chem. Eng. J. 218 (2013) 32.
[17] M. Laatikainen, K. Laatikainen, Chem. Eng. J. 287 (2016) 74.
[18] X. Li, Z. Lei, J. Qu, X. Zhou, Z. Li, Q. Zhang, RSC Adv. 7 (2017) 2002.
[19] D.M. Carmona, Á.F Cano, J.M. Arocena, Geoderma 150 (2009) 150.
[20] I. Singh, R.K. Bedi, Appl. Surf. Sci. 257 (2011) 7592.
[21] H. Xu, G. Zhu, D. Zheng, C. Xi, X. Xu, X. Shen, J. Colloid Interface Sci. 383 (2012) 75.
[22] M. Breedon, S. Zhuiykov, N. Miura, Mater. Lett. 82 (2012) 51.
[23] D.P. Singh, N. Ali, Sci. Adv. Mater. 2 (2010) 295.
[24] Z. Zhang, H. Chen, H. Che, Y. Wang, F. Su, Mater. Chem. Phys. 138 (2013) 593.
[25] Z. Zarghami, M. Ramezani, M. Maddahfar, Mater. Lett. 152 (2015) 21.
[26] R. Sharma, J.H. Kim, Y.B. Hahn, Sci. Adv. Mater. 4 (2012) 978.
[27] J. Nishio, M. Tokumura, H.T. Znad, Y. Kawase, J. Hazard. Mater. 138 (2006) 106.
[28] N.K. Dewi, I. Mubarok, A. Yuniastuti, J. Biol. Educ. 11 (2019) 289.
[29] L. Pirinejad, A. Maleki, B. Shahmoradi, H. Daraei, J.K. Yang, S.M. Lee, J. Mol. Liq. 279 (2019) 232.
[30] A.K. Shrivastava, Indian J. Environ. Prot. 29 (2009) 552.
[31] A. Saeed, M. Iqbal, M.W. Akhtar, J. Hazard. Mater. 117 (2005) 65.
[32] K.M. Joshi, B.N. Patil, D.S. Shirsath, V.S. Shrivastava, Adv. Appl. Sci. Res. 2 (2011) 445.
[33] D. Pimentel, O. Bailey, P. Kim, E. Mullaney, J. Calabrese, L. Walman, X. Yao, Environ. Dev. Sustain. 1 (19) (1999).
[34] S. Suphankij, W. Mekprasart, W. Pecharapa, Energy Proc. 34 (2013) 751.
[35] M. Ni, M.K. Leung, D.Y. Leung, K. Sumathy, Renew. Sustain. Energy Rev. 11 (2007) 401.
[36] S. Ye, R. Wang, M.Z. Wu, Y.P. Yuan, Appl. Surf. Sci. 358 (2015) 15.

[37] K. Sivula, F. Le Formal, M. Grätzel, ChemSusChem 4 (2011) 432.
[38] S.T. Huang, W.W. Lee, J.L. Chang, W.S. Huang, S.Y. Chou, C.C. Chen, J. Taiwan Inst. Chem. Eng. 45 (2014) 1927.
[39] B.L. Phoon, C.W. Lai, J.C. Juan, P.L. Show, G.T. Pan, Int. J. Hydrog. Energy 44 (2019) 14316.
[40] T. Ghodselahi, M.A. Vesaghi, A. Shafiekhani, A. Baghizadeh, M. Lameii, Appl. Surf. Sci. 255 (2008) 2730.
[41] D. Barreca, A. Gasparotto, A. Milanov, E. Tondello, A. Devi, R.A. Fischer, Surf. Sci. Spectra 14 (2007) 52.
[42] G.T.K. Swami, F.E. Stageberg, A.M. Goldman, J. Vac. Sci. Technol. 2 (1984) 767.
[43] J.A. Wani, M.S. Atone, N.S. Dhoble, S.J. Dhoble, J. Lumin. 134 (2013) 640.
[44] B. Ramesh, G. Devarajulu, B.D.P. Raju, G.B. Kumar, G.R. Dillip, A.N. Banerjee, S.W. Joo, Ceram. Int. 42 (2016) 1234.
[45] X. Gong, P. Wu, W.K. Chan, W. Chen, J. Phys. Chem. Solids 61 (2000) 115.
[46] M.G. Brik, A. Suchocki, A. Kaminska, Inorg. Chem. 53 (2014) 5088.
[47] K.W. Jung, B.H. Choi, S.Y. Lee, K.H. Ahn, Y.J. Lee, J. Ind. Eng. Chem. 67 (2018) 316.
[48] X. Zhang, X. Zhang, L. Tao, Z. Chi, J. Xu, Y. Wei, J. Phys. Chem. B 2 (2014) 4398.
[49] T. Nguyen Thi Thu, N. Nguyen Thi, V. Tran Quang, K. Nguyen Hong, T. Nguyen Minh, N. Le Thi Hoai, J. Exp. Nanosci. 11 (2016) 226.
[50] S.A. Mokhtari, M. Farzadkia, A. Esrafili, R.R. Kalantari, A.J. Jafari, M. Kermani, et al., J. Environ. Sci. Health, Part A, Environ. Sci. Eng. 14 (1) (2016).
[51] A.R. Khataee, M.B. Kasiri, J. Mol. Catal. A, Chem. 328 (8) (2010).
[52] I. Polat, S. Yılmaz, I. Altın, E. Bacaksız, M. Sokmen, Mater. Chem. Phys. 148 (2014) 528.
[53] R. Mohan, K. Krishnamoorthy, S.J. Kim, Solid State Commun. 152 (2012) 375.
[54] R. Kumar, A. Umar, G. Kumar, M.S. Akhtar, Y. Wang, S.H. Kim, Ceram. Int. 41 (2015) 7773.
[55] F. Azough, A. Gholinia, D.T. Alvarez-Ruiz, E. Duran, D.M. Kepaptsoglou, A.S. Eggeman, Q.M. Ramasse, R. Freer, Self-nanostructuring in SrTiO3: a novel strategy for enhancement of thermoelectric response in oxides, ACS Appl. Mater. Interfaces 11 (36) (2019) 32833–32843.
[56] J. Rivnay, H. Wang, L. Fenno, K. Deisseroth, G.G. Malliaras, Sci. Adv. 3 (6) (2017) 1601649.
[57] A.V.L.N. Sujith, G.S. Sajja, V. Mahalakshmi, S. Nuhmani, B. Prasanalakshmi, Neurosci. Inform. (2021).
[58] A.V.L.N. Sujith, G.S. Sajja, V. Mahalakshmi, S. Nuhmani, B. Prasanalakshmi, Neurosci. Inform. 2 (3) (2022) 100028.
[59] R.I. Doewes, L. Gangadhar, S. Subburaj, Neurosci. Inform. 1 (3) (2021) 100011.
[60] A.P. Klein, J.L. Ulmer, S.A. Quinet, V. Mathews, L.P. Mark, Am. J. Neuroradiol. 37 (6) (2016) 1005.